Brendan Ensor,[1,2] Gene Lucadamo,[3] John R. Seidensticker,[3]
Ram Bajaj,[3] Zhonghou Cai,[4] and Arthur T. Motta[1]

Characterization of Long-Term, In-Reactor Zircaloy-4 Corrosion Coupons and the Impact of Flux, Fluence, and Temperature on Oxide Growth, Stress Development, Phase Formation, and Grain Size

Citation

B. Ensor, G. Lucadamo, J. R. Seidensticker, R. Bajaj, Z. Cai, and A. T. Motta, "Characterization of Long-Term, In-Reactor Zircaloy-4 Corrosion Coupons and the Impact of Flux, Fluence, and Temperature on Oxide Growth, Stress Development, Phase Formation, and Grain Size," in *Zirconium in the Nuclear Industry: 19th International Symposium*, ed. A. T. Motta and S. K. Yagnik (West Conshohocken, PA: ASTM International, 2021), 588–619. http://doi.org/10.1520/STP162220190038[5]

ABSTRACT

Eleven Zircaloy-4 samples were irradiated in the Advanced Test Reactor at a variety of temperatures and neutron flux levels for up to 6.5 years. Subsequently, the coupons were characterized with complementary techniques to understand the mechanisms behind oxide growth as a function of different corrosion environments. Samples were examined using synchrotron X-ray diffraction/fluorescence, traditional X-ray diffraction, focused ion beam/scanning electron microscopy serial sectioning, and three-dimensional reconstruction to develop

an improved understanding of the influence of the underlying oxide microstructure on oxide growth. The oxide microstructure formed under irradiation was compared to that in samples corroded in an autoclave to discern the impact of neutron irradiation and temperature on corrosion rate, oxide kinetic transition, irradiation-induced breakaway corrosion, stress development, phase formation, and oxide grain size. The microstructure of the oxide changed with the corrosion temperature, with larger crack spacing (characteristic of kinetic transition) and larger monoclinic oxide grains formed during higher temperature corrosion. The specimens that were exposed to a neutron flux exhibited larger oxide grains and an increase in the fraction of tetragonal phase at the metal-oxide interface (but less tetragonal phase in the bulk oxide) compared to those exposed in autoclave. Data obtained from electron microscopy demonstrated the effect of irradiation and corrosion temperature on oxide morphology. One specimen underwent an irradiated-induced breakaway oxidation that was characterized by a sharp change in the corrosion rate and a decrease in the spacing between adjacent crack layers in the oxide film. Stress is hypothesized to be a key driver in the oxide growth formation, with samples nearer transition having more plastic deformation in the metal and increased elastic strain. These observations lead to a theory of oxide growth on zirconium alloys that attempts to connect and integrate the effects of stress, irradiation, temperature, phase formation, crystal orientation, porosity, and precipitate amorphization.

Introduction

Zirconium (Zr) alloys are widely used as fuel cladding in nuclear reactor cores. Zirconium alloys must have good corrosion resistance in the reactor environment where temperatures can be as high as 360°C. Although a large volume of research has been conducted into the numerous important aspects of zirconium oxide growth, questions still remain as to the basic corrosion mechanisms in these alloys. This is further complicated by the environment in which these alloys are usually tested, which is different from the environment in which they have to perform. During service, zirconium alloys are subject to high levels of radiation, including gamma, beta, and neutron radiation. The exposure to neutron flux can impact corrosion, by modifying the properties of the base metal, the properties of the oxide layer, or the concentration of radiolytic species in the coolant. Examinations have shown that corrosion accelerates in high burnup material, which could be caused by accumulated neutron fluence.[1–4] This acceleration can cause the corrosion rate to be up to thirty times higher than the corrosion rate outside the reactor.[5] There are many examples of how irradiation with neutrons can affect corrosion performance.[1–3,6,7] Some studies suggest it is the changes to the microstructure or microchemistry of alloying elements that are most important to irradiation acceleration

of corrosion.[1,4,8] The focus of this study is on the effects of neutron fluence on the oxide microstructure and how it may be influenced by the irradiated alloy microstructure.

Because stress stabilizes tetragonal-phase oxide grains, the tetragonal phase can be used as a marker for stress at the metal-oxide interface, as has been seen and proposed previously.[9,10] While the tetragonal fraction has been measured on autoclave samples of Zr alloys using microbeam synchrotron radiation, little data exist on neutron irradiated oxide samples.[9,11–13]

Neutron damage in Zr alloys creates defects in the crystal structure of the metal, causing the yield strength of the alloys to increase and the ductility to decrease.[14] The yield strength increase is more pronounced when irradiated at lower temperatures; this is noteworthy because it has been observed that alloys corroded in reactor to high neutron fluence at low temperatures exhibit a relatively higher increase in corrosion rate than those at higher temperatures.[5,14,15] One possible mechanism for corrosion acceleration is that as the material becomes harder, it becomes less able to accommodate the growth stresses in the oxide, leading to higher stresses at the metal-oxide interface and earlier oxide transition. This is more severe at lower corrosion temperatures, consistent with the increase in yield stress as a function of temperature.[14] The irradiation-induced creep of the material is another attribute that could affect this mechanism, with material that has a higher creep rate becoming softer and more able to accommodate oxide growth stresses.[16]

Another effect thought to be a possible cause of accelerated corrosion in reactors is the redistribution of alloying elements from second-phase precipitates into the matrix.[1,4,8,17–19] The alloying elements are thought to play a key role in stabilizing oxide growth. The effects of alloying element redistribution under irradiation (which can alter the corrosion potential in the oxide layer[20]), combined with an increasingly less ductile metal caused by irradiation hardening, leads to the following reasoning on corrosion under irradiation. In brief, redistribution of alloying elements causes unstable oxide growth, which leads to build up of stresses and eventual breakdown of the protective oxide layer, which is exacerbated by less accommodation of oxide growth stresses due to the hardening of the metal.

Experimental and Materials

Eleven samples of irradiated, alpha-annealed Zircaloy-4 were corrosion tested in the Advanced Test Reactor at the Idaho National Laboratory in the same manner as previously described.[5] Samples of the oxide layers formed under these conditions were examined at the 2-ID-D beamline at the Advanced Photon Source (APS) at Argonne National Laboratory using microbeam synchrotron radiation diffraction and fluorescence. The samples examined are listed in table 1. The samples were corroded at a range of temperatures (272°C to 355°C), a range of neutron flux levels (0 to 11.5×10^{13} n/cm^2/s, E > 1 MeV), and to a variety of oxide thicknesses (1.6 µm to 29.3 µm). Figure 1 shows the weight gain as a function of time for all eleven

TABLE 1 Zircaloy-4 neutron-irradiated samples examined using the 2-ID-D beamline at the APS

Sample Designation	Avg. Flux (10^{13}n/cm^2/s) E>1 MeV	Total Fluence (10^{20}n/cm^2) E>1 MeV	Exposure Time (Days)	Average Corrosion Temperature	Oxide Layer Thickness
H1169J	1.9	24.8	1,474	272°C	1.97 µm
H1193J	1.9	24.8	1,474	272°C	2.47 µm
H1490J	8.3	81.5	1,138	274°C	1.60 µm
H381J	10.5	217.1	2,395	272°C	15.8 µm
H977J	4.2	44.1	1,206	314°C	25.1 µm
H944J	6.1	25.6	487	339°C	15.8 µm
H1240J	2.4	24.2	1,189	337°C	29.3 µm
H337J	0	0	1,139	355°C	25.6 µm
H421J	1.4	6.8	573	355°C	25.7 µm
H657J	8.1	16.1	230	352°C	9.50 µm
H920J	11.5	32.5	328	353°C	21.8 µm

FIG. 1 Weight gain data from eleven neutron-irradiated Zircaloy-4 coupons corroded at various temperatures and under different fluxes as indicated.
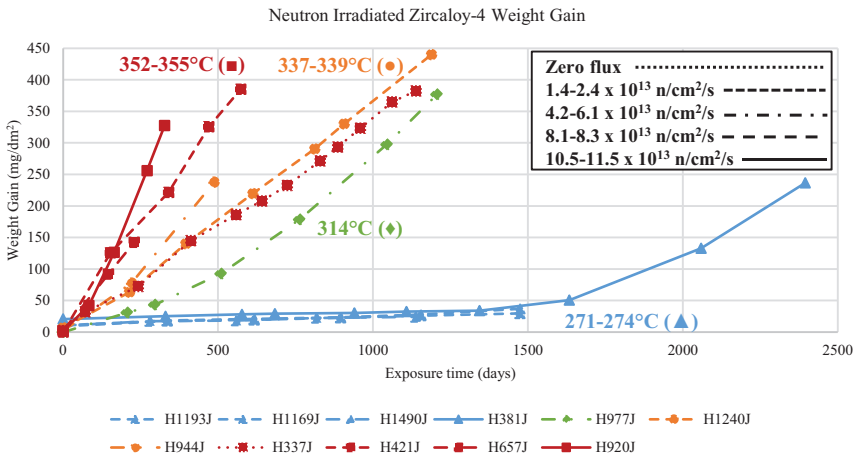
irradiated Zircaloy-4 samples tested in this study. Samples were examined at the end of their exposures.

SYNCHROTRON X-RAY ANALYSIS

Because the samples were radioactive, they required encapsulation for examination at the APS (the collective radioactivity was 18.5 µCi with contact dose rates up to 0.07 mGy/h). The samples were wrapped in aluminum foil, put into a stainless steel tube, and mounted in Bakelite, as shown in **figure 2**.
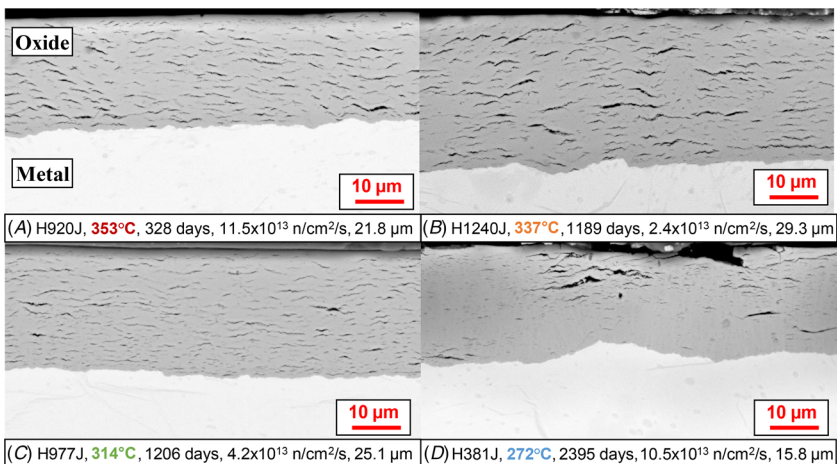
FIG. 2   Examples of sample preparation on two irradiated Zircaloy-4 samples, on the left is H421J and on the right is H1240J.
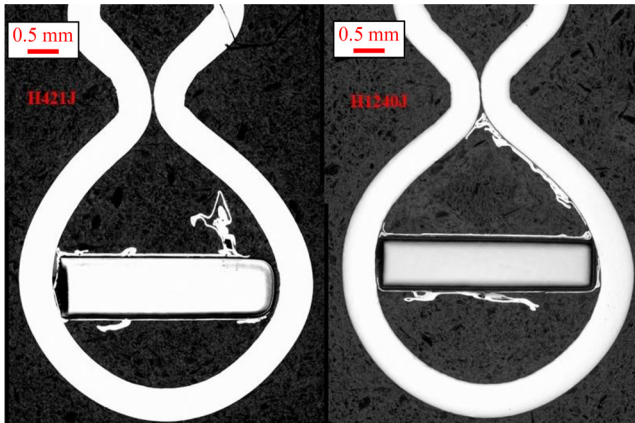
Slices were taken of the Bakelite-mounted samples and polished to a mirror finish. **Figure 3** shows four examples of scanning electron microscope (SEM) micrographs of the samples.

After the samples were polished, they were attached to aluminum (Al) studs (identical to those used at the 2-ID-D beamline) using superglue, encapsulated in a Kapton tube, and secured to the Al stud using Kapton tape. These samples were

FIG. 3   SEM images of the oxide layers formed on four of the Zircaloy-4 samples listed in **table 1**.

(A) H920J, 353°C, 328 days, 11.5x10^{13} n/cm^2/s, 21.8 µm

(B) H1240J, 337°C, 1189 days, 2.4x10^{13} n/cm^2/s, 29.3 µm

(C) H977J, 314°C, 1206 days, 4.2x10^{13} n/cm^2/s, 25.1 µm

(D) H381J, 272°C, 2395 days, 10.5x10^{13} n/cm^2/s, 15.8 µm

then placed in a container and shipped to Argonne National Laboratory for examination at the APS at the 2-ID-D beamline. The samples were examined in the same manner as the nonirradiated cross-sectional samples described in previous work.[9] The samples were mounted at the beamline and tilted into the beam's path. The beam energy was 8.34 keV (providing diffraction from planes with d-spacings between $\sim$ 2 to 4 Å) and translated in 0.25-μm steps across the oxide thickness while simultaneously X-ray fluorescence (XRF) and diffraction data were acquired. At least one X-ray diffraction (XRD) scan across the oxide thickness was performed on each sample, more often two. For one sample (H1490J), an XRD and XRF map of 6 μm by 5 μm was acquired. One added difficulty during these experiments was the unforeseen attenuation of the photons through the Kapton. This was not an issue for the incoming X-ray beam and the outgoing diffracted X rays as their energy was sufficiently high; however, at the L edges of the Zr ($\sim$ 2.2 to 2.5 keV) enough beam absorption occurred as to make it difficult to use the Zr fluorescence signal to determine position in the oxide layer as done previously. Instead, this was achieved by using the tin (Sn) L line and using diffraction patterns (for determining whether the beam was on the oxide layer or on the metal). Although this added some uncertainty to the determination of the beam position, this was compensated by using longer acquisition times. Sample data processing and analysis techniques were similar to those described previously.[9] Errors for determination of grain size and tetragonal fraction were typically low due the use of the high-intensity synchrotron source, subsequent peak intensities, and good peak fitting, estimated at $< \pm 1$ nm (monoclinic) or $< \pm 3$ nm (tetragonal) and $< \pm 0.01$, respectively (and not shown to improve figure readability).

FOCUSED ION BEAM SERIAL SECTIONING AND SCANNING ELECTRON MICROSCOPE IMAGING OF METALLOGRAPHIC CROSS SECTIONS

Serial section tomography was performed on some of the samples examined at the APS. The pieces were roughly 3 mm by 6 mm by 1 mm in size. Pieces were affixed to an SEM stub and sputter-coated with gold. The "U-trench" method was used as the basis for the serial section experiments. Areas selected for serial sectioning were first masked by depositing a 12 by 12 μm^2 to 16 by 16 μm^2 carbon layer that was 1.2 to 1.5 μm thick. The area around the mask was milled away, resulting in a peninsula of material that was then sectioned. The slice thickness was set to 50 nm with a total of 118 to 250 slices acquired per specimen. Secondary and backscatter electron (BSE) images were acquired using an accelerating voltage of 10 kV with tilt correction and dynamic focus settings enabled to compensate for the stage tilt and change in focal plane, respectively. Subsequent image processing and analysis was performed using Avizo (Thermo Fisher Scientific) software. The individual images in the section were processed to remove any curtaining and to reduce noise and intensity variations.

Backscatter SEM images were obtained from a select number of the specimens that were prepared in cross section for the APS experiments. Imaging was

performed at 20 kV in a dedicated field emission gun SEM. The samples chosen had similar oxide thicknesses (between about 12.5 µm and 25 µm) after exposure in the Advanced Test Reactor.

The samples were examined with grazing angle XRD from 26 to 39° 2θ on a PANalytical Multipurpose Diffractometer using copper (Cu) Kα X-ray radiation operated at 45 kV/40 mA. This angular range encompasses the primary diffraction peaks of monoclinic and tetragonal zirconium dioxide (ZrO_2). The instrument was configured using a polycapillary lens bundle with a 0.3 radian incident convergence, 1/16° divergence slit, 0.27° parallel plate collimator, and a proportional detector. The crystalline phases were identified by comparison of the measured diffraction patterns to reference patterns in the International Centre for Diffraction Data powder diffraction file (PDF) 4+ 2013 database. The system alignment was verified by observed diffraction peaks from a silicon (Si) reference standard (NIST SRM 604E). Incidence angles of 1°, 2.5°, and 4° were used, which correspond to penetration depths of ∼1 to 5 µm in ZrO_2, with more penetration for higher angles of incidence.

Results and Discussion

APS X-RAY DIFFRACTION

The primary diffraction peaks observed in the examination of oxide layers were identified as coming from the monoclinic oxide phase, including the $(-111)_m$, $(111)_m$ peaks, and the $\{110\}_m$ and $\{200\}_m$ families of peaks. Minor diffraction peaks were also identified that matched previous observations on nonirradiated samples.[9] The primary peak associated with the tetragonal phase observed was the $(101)_T$, found on the low 2θ side of the $(111)_m$ peak. As before, the tetragonal peak location did not exactly match the literature value.[13] An additional peak associated with the tetragonal phase was visible in the diffraction patterns taken from the metal-oxide interface, which could be indexed as the $(002)_T$ peak (∼32.7° 2θ in these experiments), in agreement with previously reported observations.[11] Peaks associated with the suboxide phase were detected in the metal close to the metal-oxide interface as it was in the samples corroded in autoclave.[9]

Figure 4 shows examples of the diffraction patterns obtained during the scan of the oxide layer in a sample (H381J) obtained both from the metal (top) and from the oxide layer (bottom). The zirconium metal appears as spots with high intensity (characteristic of large metal grains), while the zirconium oxide appears as rings with some lobes of higher intensity (characteristic of a textured, small grained oxide layer). The monoclinic oxide peaks are arrowed in red and the tetragonal peak in blue and denoted by "m" and "T," respectively. The lighter region on the left side of the diffraction pattern is caused by obstruction of the fluorescence detector, which needed to be placed immediately adjacent to the sample to obtain sufficient fluorescence intensity to determine position. The strong diffraction ring intensity at low 2θ (labeled "artifact") does not come from the sample and its origin could not be

FIG. 4 Synchrotron X-ray diffraction patterns of irradiated Zircaloy-4 sample H381J; (top) pattern obtained in the metal and (bottom) pattern obtained in the oxide.
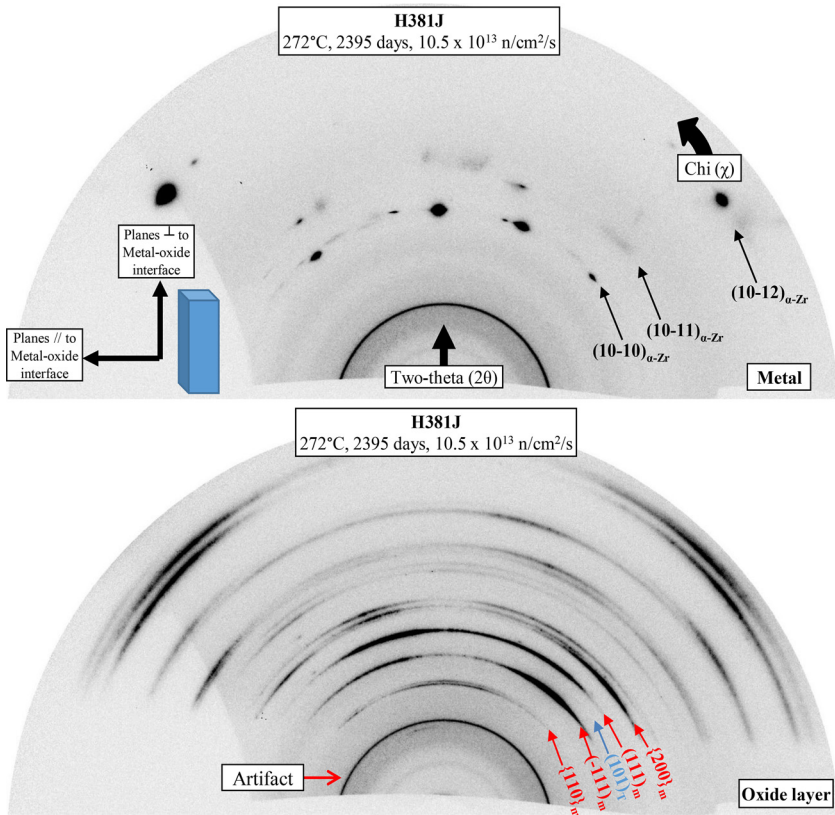

determined. The peaks at higher 2θ could all be indexed as belonging to monoclinic oxide.

As mentioned previously, the $(002)_T$ peak was observed in some patterns from the metal-oxide interface. Consistent with previous observations, the $(002)_T$ peak appears as a highly strained diffracted intensity in the vicinity of the $\{200\}_m$ peaks. Figure 5 shows a diffraction pattern obtained at the metal-oxide interface (from sample H657J), with the $(002)_T$ peak highlighted.

The diffraction intensity associated with the $\{200\}_m$ family of peaks was consistent with the presence of columnar monoclinic oxide grains oriented in the growth direction of the oxide, with the $(200)_m$ peak approximately parallel to the metal-oxide interface, as previously reported.[9,11] The $(020)_m$ and the $(002)_m$ peaks were located at χ angles consistent with planes more perpendicular to the metal-oxide interface, and the $(200)_m$ peak was located at χ angles consistent with planes more

FIG. 5 Synchrotron X-ray diffraction pattern of irradiated Zircaloy-4 sample H657J obtained near the metal-oxide interface; the $(002)_T$ peak is highlighted with a blue circle and other major oxide peaks with red and blue arrows for monoclinic (denoted by "m") and tetragonal (denoted by "T") oxide peaks, respectively.
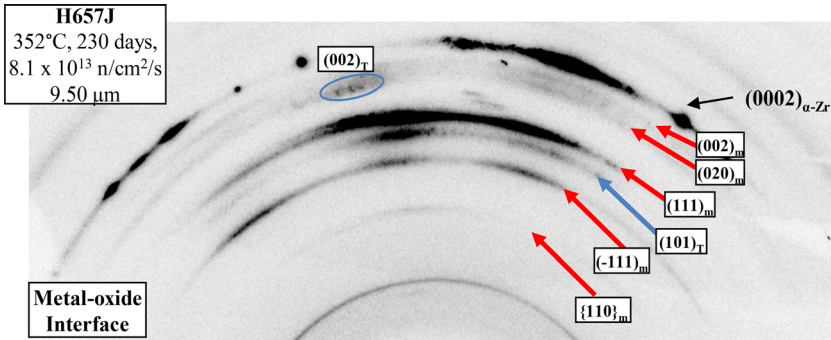
parallel to the metal-oxide interface. **Figure 6** shows a diffraction pattern from an irradiated Zircaloy-4 sample (H977J) obtained in the oxide layer away from the metal-oxide interface and illustrates the χ angles where the $\{200\}_m$ peaks were observed. For such a geometry, the $(020)_m$ and $(002)_m$ peaks would appear close to the 12 o'clock position while the $(200)_m$ intensity should appear closer to the equator (in this case at $\sim$ 10 o'clock), as observed.

The 2θ locations of the major monoclinic oxide diffraction peaks match well with the PDF locations (PDF #05-0665, #37-1484, #42-1164, and #22-1025), as also

FIG. 6 Synchrotron X-ray diffraction pattern of irradiated Zircaloy-4 sample H977J obtained at the metal-oxide interface; the location of the $\{200\}_m$ family of peaks are highlighted with red arrows with the $(002)_m$ and $(020)_m$ generally appearing at a χ angle consistent with planes perpendicular to the metal-oxide interface and the $(200)_m$ appearing at a χ angle consistent with planes approximately parallel to the metal-oxide interface.
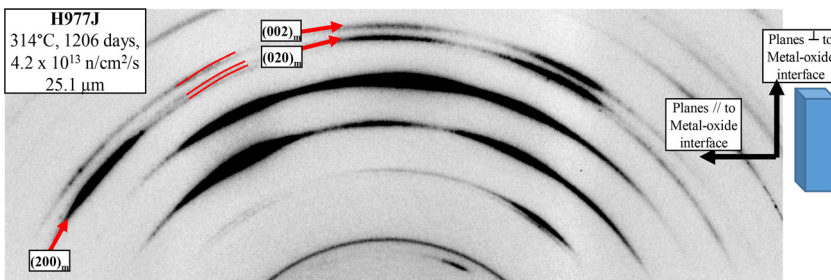
observed in autoclave corroded samples.[9] Consistent with the observations in auto-clave corroded samples is the variation in the intensities of the diffraction peaks as a function of distance from the metal-oxide interface. The major monoclinic oxide peaks exhibit seemingly periodic variations that occur over a distance consistent with the amount of oxide grown within a transition cycle.[12] The increase in the calculated tetragonal fraction (described later in this paper) comes from both an increase in the intensity of the $(101)_T$ tetragonal peak and a decrease in the intensity of the $(111)_m$ and $(-111)_m$ monoclinic peaks.[9] The only noteworthy differences in the diffraction patterns from the oxide layers formed under neutron irradiation were (i) the high intensity of the $(101)_T$ tetragonal peak at the metal-oxide interface (such as seen in **fig. 5**), which increased with neutron fluence, and (ii) the change in full-width half-maximum of the monoclinic diffraction peaks within an oxide layer.

The diffraction results presented here and in previous work on nonirradiated samples fit with previous descriptions of oxide growth on zirconium alloys.[9,11] The model used here to interpret the results includes the basics of protective oxide layer growth and is consistent with the findings from the examination of oxide layers formed in both autoclave testing and in-reactor corroded samples. The oxide growth can be split into four distinct phases:

(1) Oxide nucleation
(2) Growth of the protective oxide layer (i.e., barrier layer)
(3) Breakdown of the protective oxide at oxide transition and the formation of a new barrier layer
(4) Irradiation-induced transition (distinct from the cyclic transition process described in Steps 1 to 3) to post-transition oxide growth

During (1), the oxide nucleates as small, equiaxed grains, postulated to be driven partly by matching to the metal lattice and minimization of stress in the oxide.[11] The oxide layer formed during this phase exhibits equiaxed oxide grains, higher tetragonal fraction (f_T) than during subsequent oxide growth, a thinner sub-oxide layer, and more uniform grain size (larger tetragonal-phase grains and smaller monoclinic-phase grains) as compared to oxide grown in the next phase.

During (2), favorably oriented monoclinic grains (i.e., those oriented with the $(200)_m$ plane along the oxide growth direction) grow into larger, columnar oxide grains, driven by the need to reduce stress accumulation. The oxide layer formed during this phase shows a lower f_T (which increases as the oxide approaches transition), a significant suboxide layer (the size of which increases as transition is approached and oxide growth slows), and a divergence in the grain size of the monoclinic and tetragonal phases (monoclinic grains become larger, while tetragonal grains transform to the monoclinic phase above a critical size).

During (3), the oxide transition, the protective nature of the oxide layer is lost, likely when a critical stress is reached causing breakdown in the protective nature of the oxide. Because the cracking is horizontal, it has been proposed that such cracks cause an interconnection of previously existing porosity.[11] This leads to easy access

of the metal to the oxidizing species, which is made possible by the oxide breakup leading to a percolation of porosity.[1,11]

Phases (1) and (2) are governed by the corrosion rate and, currently, there are efforts to model this behavior based on the potential across the oxide and space charge compensation.[21] Phase (3), oxide transition, is governed by stress accommodation and the pressure of a critical stress of the protective oxide layer. The first three phases have their properties determined by the alloying elements and the properties of second-phase particles (SPPs).

Phase (4), an irradiation-induced transition to enhanced corrosion rates, is described well by Kammenzind et al. for Zircaloy-4 and appears to be related to a synergistic effect between thick oxide films and irradiation effects on SPPs as well as alloying element redistribution.[5,8] Additional accelerating factors, such as acceleration due to hydrogen concentration, can also impact the corrosion rates observed in this regime.[22]

With such a qualitative model, and defined characteristics of the important phases of oxide growth, it becomes possible to hypothesize how changing environmental and material conditions can impact corrosion behavior, including a change in corrosion temperature, accumulation of hydrides, or exposure to neutron and gamma irradiation. In the following sections, the effect of neutron irradiation on oxide growth characteristics will be explored as it relates to this model.

DETERMINATION OF GRAIN SIZE ON IRRADIATED ZIRCALOY-4 OXIDE LAYERS FROM MICROBEAM SYNCHROTRON X-RAY DIFFRACTION

The diffraction patterns for the oxides obtained were integrated to create a plot of diffracted intensity versus 2θ.[9] These patterns were individually fit and analyzed to determine the grain size from peak broadening using the Debye-Scherrer formula, shown in equation (1), which calculates the grain size d from the full-width half-maximum of the peaks discerned from the fitted diffraction patterns.[13]

$$d = \frac{0.9\lambda}{B_\Theta cos\Theta} \quad \text{where} \quad B_\Theta = (B^2 - B_i^2)^{1/2} \tag{1}$$

where B is the measured peak full-width half-maximum in radians, and B_i is the instrumental broadening, which was measured to be 0.051 radians in this beamline using an LaB_6 standard. Note that only size broadening is considered.

Figure 7 shows the average grain size calculated from oxide peaks in the diffraction patterns taken in the oxide layer (corresponding to the width of the columnar monoclinic grains and to the diameter of the equiaxed tetragonal grains) for the $(111)_m$ and $(101)_T$ orientations, calculated from the peak broadening for the scans performed in this study, separated by the corrosion temperature. The data in figure 7 correspond to the average values calculated from equation (1) from multiple scans on one sample. Samples with very thin oxide layers are not considered (because near-interface effects play a role, as previously described[9]). As discussed in previous work on nonirradiated specimens, nonuniform strain could also contribute to

FIG. 7   Average grain size of the monoclinic, $(111)_m$, and tetragonal, $(101)_T$, phases of irradiated Zircaloy-4 samples with > 9 μm of oxide.
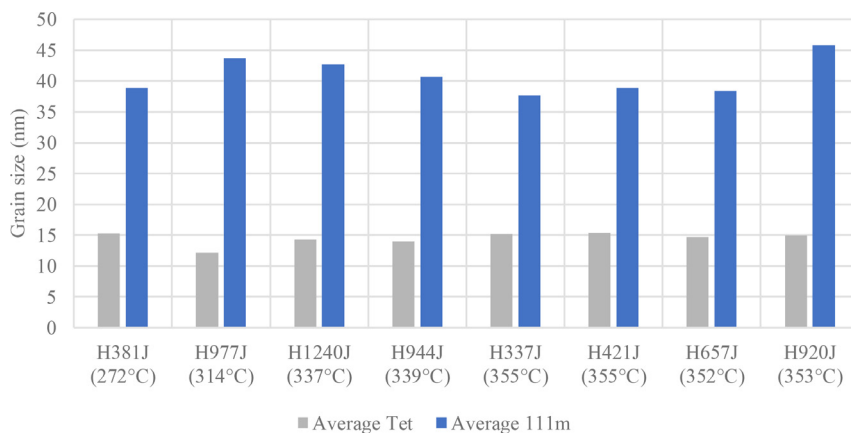
broadening the diffraction peaks and causing the calculation of the grain size to be smaller than the actual value.[9] A Williamson-Hall analysis was not performed in this study, but previous analysis indicates that most of the observed peak broadening comes from size effects.[12]

The tetragonal-phase grain size lies within a band between 12 and 15 nm, while the monoclinic-phase size is within a band of about 37 to 47 nm. In the samples tested in an autoclave,[9] the monoclinic grain size increased with temperature, most markedly in the higher temperature range of 400°C to 454°C steam, an environment absent from this study. Between 272°C and 355°C, a temperature dependence on grain size is not readily evident for the samples corroded under irradiation, as shown in figure 7. There was, however, an increase in the monoclinic grain size with increasing neutron flux. This can be seen in figure 8, which shows the monoclinic oxide grain size from samples in the lowest temperature band (271 to 274°C) and highest temperature band (352 to 355°C) as a function of the average neutron flux to which the particular sample was exposed. When examining samples at a low neutron flux level ($\sim 2 \times 10^{13}$ n/cm^2/s), there was an observed increase in monoclinic oxide grain size from 272°C (37.1 nm) to 355°C (39.7 nm), consistent with previous observations in an autoclave.[9] At higher neutron flux levels, the effect of the flux appears to dominate over the effect of temperature on the monoclinic grain size.

Figure 9 shows the oxide grain sizes calculated from the broadening of the $(111)_m$ and $(101)_T$ peaks from all samples and averaged across all scans obtained for each temperature as a function of distance from the metal-oxide interface.

The samples exposed to different neutron fluxes (and neutron fluences) are shown using different line styles while the corrosion temperature is shown in

FIG. 8   Average grain size of the $(111)_m$ oxide peak of irradiated Zircaloy-4 samples from the outer 2 μm of oxide overlaid with the average neutron flux with which the samples were exposed.
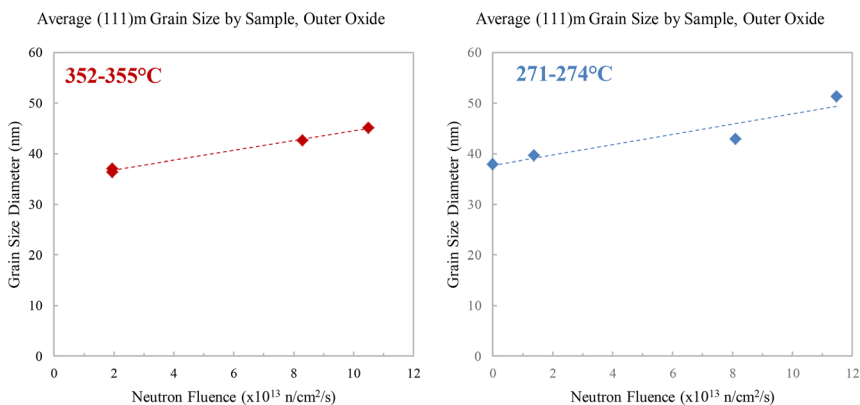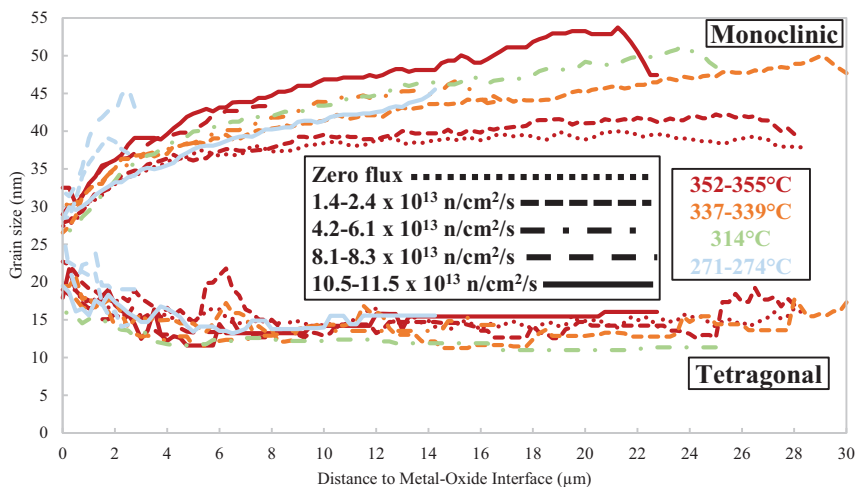

FIG. 9 $(111)_m$ grain size (top) and $(101)_T$ grain size (bottom) averaged for all scans taken from irradiated Zircaloy-4 samples as a function of distance from the metal-oxide interface; the line color indicates temperature and the line style indicates level of neutron flux as indicated in the legend.


different colors, as specified in the legend. As observed in the autoclave samples studied previously, the tetragonal grain size *decreases* from the metal-oxide interface to about 6 μm into the oxide layer, while the monoclinic grain size *increases*

more or less continuously.[9] The monoclinic grain sizes at locations far from the metal-oxide interface are in the 40 to 50 nm range, while the tetragonal grain size is about 15 nm, similar to what was seen in the samples corroded in an autoclave. No change in the tetragonal-phase grain size was observed as a function of neutron flux or fluence. As discussed in previous studies on nonirradiated samples, the equiaxed grains of tetragonal oxide phase have been reported to be unstable above a certain size, approximately 15 nm.[9,11,13] As the tetragonal grains grow above the critical size, they transform into the monoclinic phase; thus, only the smaller (< 15 nm) tetragonal grains remain. This explains the apparent decrease of tetragonal grain size with oxide thickness.

In contrast with the autoclave corroded samples, the monoclinic-phase grain size continues to increase toward the oxide-water interface in the samples exposed to irradiation. Note that the only sample in which the monoclinic grain size does not increase toward the oxide-water interface is the sample that was not irradiated (H337J, shown as a dotted line in fig. 9). This suggests that exposure to the neutron flux increases the size of the monoclinic oxide grains, that is, the oxide columns become wider as the reactor exposure increases. Figure 10 shows only the samples corroded between 352°C and 355°C, demonstrating the separation in the mono-clinic grain size that occurs with increasing neutron flux.

These results represent a measurable change affected by neutron irradiation on monoclinic oxide grain size. The questions are then: What causes the increase in oxide grain size and what role might this play in the corrosion process? To answer the latter question, a comparison is warranted between figure 1 (which shows the weight gain of the irradiated Zircaloy-4 samples) and figure 10, particularly between samples corroded

FIG. 10 $(111)_m$ grain size (top) and $(101)_T$ grain size (bottom) averaged between scans for irradiated Zircaloy-4 samples as a function of distance from the metal-oxide interface corroded at temperatures between 352 and 355°C; line style indicates the neutron flux.
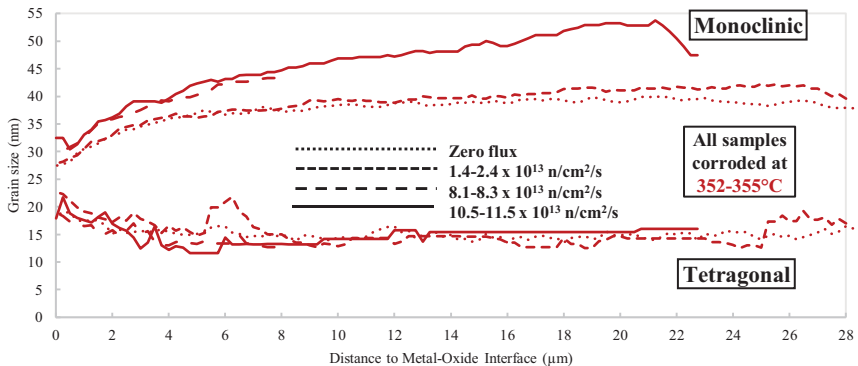
out of flux at 355°C, H337J (dotted) and H421J (1.4×10^{13} n/cm^2/s, short dashed). These samples show little difference in monoclinic grain size but substantial difference in corrosion kinetics. This would indicate that the oxide grain size, in this case, does not substantially affect the corrosion rate acceleration observed under neutron irradiation and thus might have little effect on corrosion acceleration due to neutron exposure. Because the age of the oxide increases with distance from the metal-oxide interface, the neutron fluence increases from left to right in figure 10. This indicates that the exposure to neutron flux increases the monoclinic oxide grain size.

DETERMINATION OF TETRAGONAL FRACTION ON IRRADIATED ZIRCALOY-4 OXIDE LAYERS FROM MICROBEAM SYNCHROTRON X-RAY DIFFRACTION

If exposure to neutron irradiation causes an increase in oxide grain size, then it would be expected to see both the tetragonal and monoclinic phase increase in grain size. Because it has been shown that the tetragonal phase is not stable above approximately 15 nm, the increase in grain size would be expected to decrease the tetragonal-phase fraction with increasing neutron fluence as tetragonal grains increase in size above the stable threshold and transform to monoclinic.[9] The tetragonal fraction, f_T, was calculated from the curve fits of the diffraction patterns using the Garvie-Nicholson formula, as shown in equation (2), where each term is the integrated area of the specific diffraction peak of the oxide phase denoted.[23]

$$f_T = \frac{I(101)_T}{I(101)_T + I(\bar{1}11)_m + I(111)_m} \qquad (2)$$

Figure 11 shows the average tetragonal fraction for irradiated Zircaloy-4 samples with oxide thicknesses greater than 2.5 μm and that were examined using

FIG. 11   Average tetragonal fraction for irradiated Zircaloy-4 samples as a function of distance from the metal-oxide interface; color indicates corrosion temperature and line style represents neutron flux.
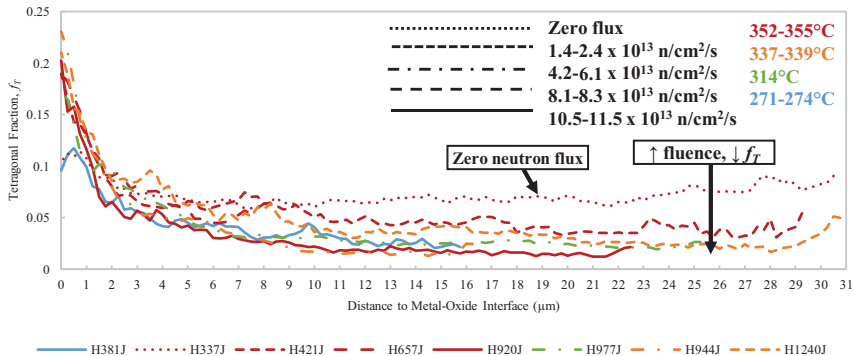
synchrotron radiation as a function of distance from the metal-oxide interface. The results show that the overall tetragonal oxide fraction decreases with increasing fluence in the bulk oxide (far from the metal-oxide interface).

The corrosion temperature has little effect on the tetragonal fraction, consistent with previous results[9] and benchtop XRD results. Figure 12 shows diffraction intensity versus position (2θ) acquired using benchtop XRD for two samples with exposure to similar levels of neutron flux (10.5 to 11.5×10^{14} n/cm^2/s) but at two different corrosion temperatures (272°C/dashed line and 353°C/solid line), highlighting the similar diffraction peak intensities for all three constituent peaks of the Garvie-Nicholson formula (equation [2]) for tetragonal fractions in the outer oxide. Each sample has at least 15 μm of oxide, and scans were performed at grazing angles of 1° and 2.5° with penetration of only a few micrometers of outer oxide. Note that the samples examined with benchtop XRD were examined in frontal geometry as opposed to in cross section (which is the geometry of the samples examined using μXRD at the APS).

One noticeable difference among the samples in figure 11 is that the tetragonal fraction in the sample that experienced no neutron flux (H337J) is nearly double the f_T in the bulk oxide as compared to the samples that were corroded under a neutron flux. Figure 13 highlights this difference by showing the average f_T from scans taken from the four samples corroded at 352 to 355°C as a function of distance from the metal-oxide interface. As can be observed, the higher the neutron fluence, the lower the f_T is at a given distance from the metal-oxide interface.

FIG. 12   X-ray diffraction intensity versus position (2θ) for two Zircaloy-4 samples exposed to similar neutron flux (10.5 to 11.5×10^{14} n/cm^2/s) but at two different corrosion temperatures (272°C and 353°C). Each sample has at least 15 μm of oxide and scans were performed at grazing angles of 1° and 2.5° with penetration of only a few micrometers of outer oxide. Arrows point toward the diffraction peaks that constitute the formula for f_T.
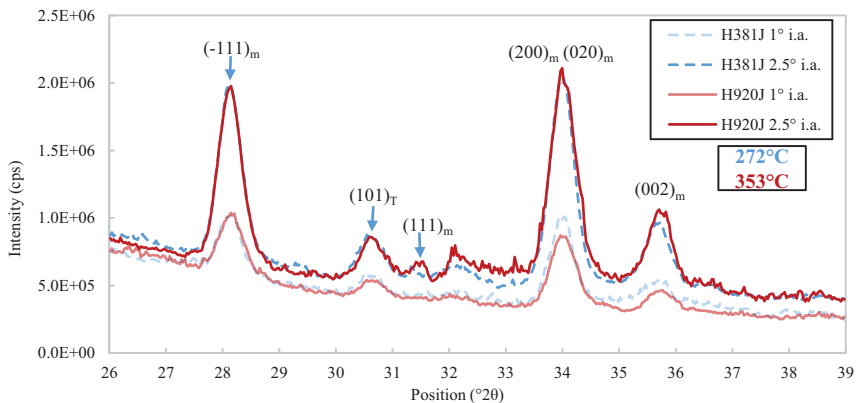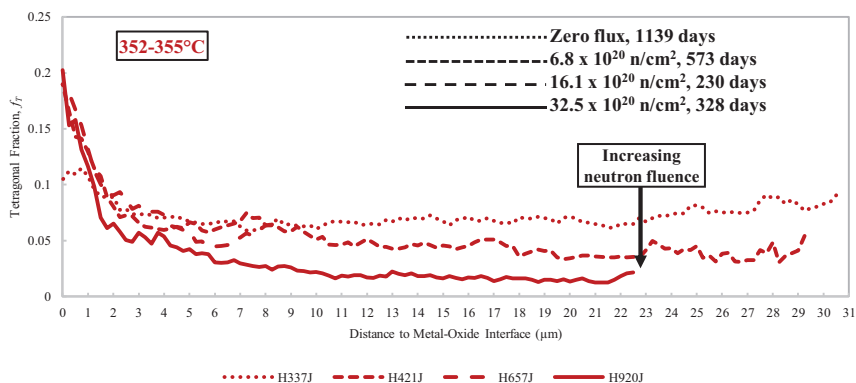
FIG. 13   Average tetragonal fraction for irradiated Zircaloy-4 samples corroded at 352 to 355°C as a function of distance from the metal-oxide interface; line style represents neutron fluence.

Again, the decrease of f_T in the bulk oxide with increasing neutron fluence is consistent with the observations on the change in oxide grain size. When the tetragonal-phase grain size increases above the critical size for stability (~ 15 nm), it transforms to the monoclinic phase. As a result, f_T is lower for samples with higher neutron fluence as an increase in the size of tetragonal grains above the critical size leads to transformation to monoclinic. Exposures up to ~ 33 dpa were included in this test.

The effect of the neutron irradiation on f_T is not limited to the bulk oxide. The maximum f_T value near the interface appears to be higher for samples with higher neutron fluence. Figure 14 shows the maximum values of the tetragonal fraction as a function of neutron fluence. The maximum value of f_T occurs at the metal-oxide interface. Thus, the f_T is lower in the bulk oxide but higher at the metal-oxide interface for higher neutron fluence.

The tetragonal phase is stabilized by a number of factors, including grain size, presence of alloying elements, and stress.[24] Grain size can be eliminated as a cause of the increase in f_T at the metal-oxide interface in this study because, as shown in figure 7, the tetragonal grain size at the metal-oxide interface is the same for each level of neutron flux. Although it is possible that the redistribution of iron (Fe) out of the SPPs would increase the concentration of alloying elements in the matrix, the amount of Fe is small in comparison to the Sn already present in solution, and thus this effect is unlikely to cause the large increase in f_T. It is instead hypothesized that radiation hardening of the metal leads to a decrease in stress accommodation of the oxide growth, which would cause an increase in stress and an increase in f_T with neutron fluence. Irradiation hardening of Zircaloy-4 begins to level off at $\sim 30 \times 10^{20}$ n/cm^2 (~ 4 to 5 dpa).[14]

FIG. 14   Maximum (circles) and bulk (squares) values of tetragonal fraction of irradiated
Zircaloy-4 samples as a function of neutron fluence; a fit of a second-order
polynomial is given for each set of data.

Tetragonal Fraction (Bulk and Max) vs Fluence
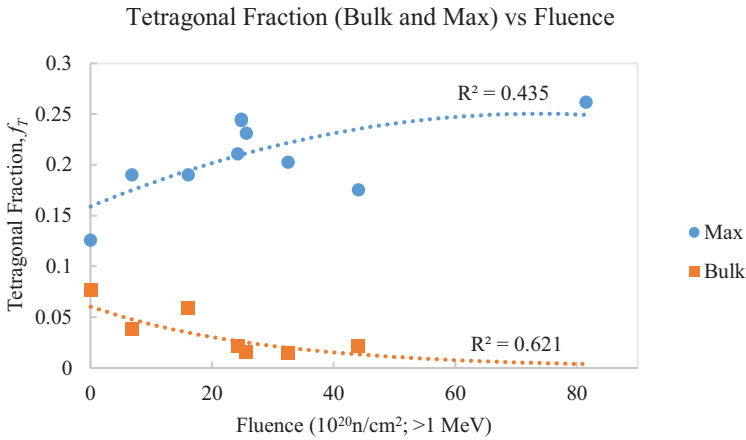
The material examined here is recrystallized alpha-annealed Zircaloy-4. Although not examined in this study, it would be expected based on the irradiation-induced creep rate differences between recrystallized alpha-annealed Zircaloy-4 (lower creep rate) and cold-worked, stress-relief annealed Zircaloy-4 (higher creep rate) that less tetragonal phase would be present at the interface for cold-worked, stress-relief annealed Zircaloy-4 due to the higher creep rate causing the metal substrate to be able to accommodate more oxide growth stresses.[16]

ANALYSIS OF FLUORESCENCE AND XRD MAP ON AN IRRADIATED ZIRCALOY-4 SAMPLE

To compare the behavior of irradiated Zircaloy-4 to autoclave corroded Zircaloy-4, an XRD and fluorescence map, as was done previously,[9] was acquired on sample H1490J (irradiated at 8.3×10^{13} n/cm^2/s, for 1,138 days, at 274°C, forming an oxide layer of 1.60 μm). The intensity of the $(111)_m$ and $(-111)_m$ peaks increase from the oxide-water interface to approximately 1 μm from the metal-oxide interface, at which point they decrease, but the $(101)_T$ diffraction intensity increases. **Figure 15A** through **C** shows the diffraction intensity maps for these three oxide peaks. The variation in the intensity of these peaks (red being the highest, blue being the lowest, as indicated by labels, respectively) leads to the familiar evolution of f_T. **Figure 15D** shows a map of the distribution in the calculations of f_T using the Garvie-Nicholson formula (equation [2]) and the intensities of the maps in A through C.

The distribution of f_T with distance from the metal-oxide interface was remarkably similar for the entire map. The f_T is low in the bulk oxide but increases to a higher value at the metal-oxide interface, which is consistent with the results in the
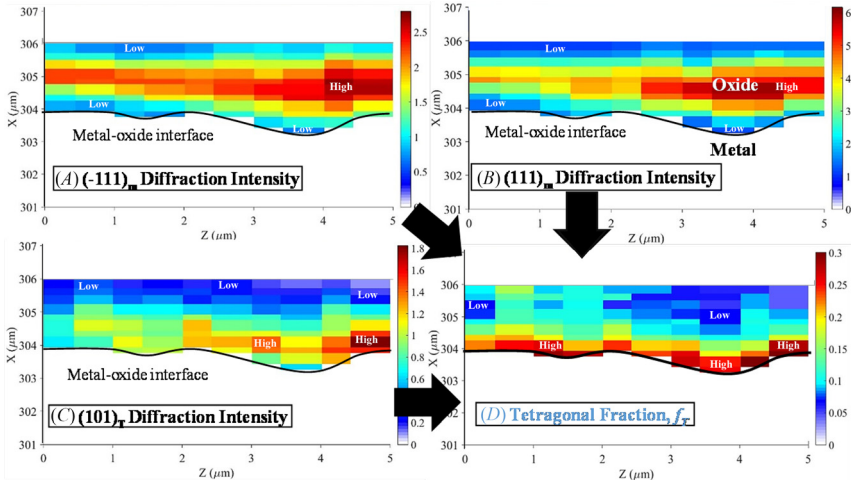
previous section. The much-sharper change in the tetragonal fraction is different from that observed in a previously examined nonirradiated sample, which can be observed in figure 16 of Ensor et al.[9] The relatively high value of f_T at the interface was not surprising as this sample was exposed to a neutron fluence of 81.5×10^{20} n/cm^2. Figure 16 shows the distribution, left, and the average, right, of the values of f_T as a function of distance from the metal-oxide interface.

The values of f_T at the interface varied somewhat from scan to scan. This variation correlated with increased oxide thickness in that location. Figure 17 shows the
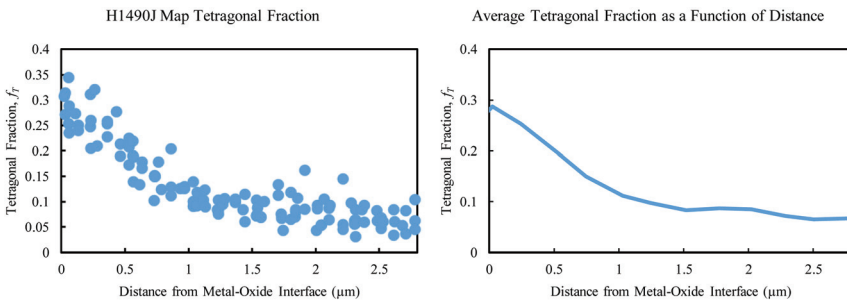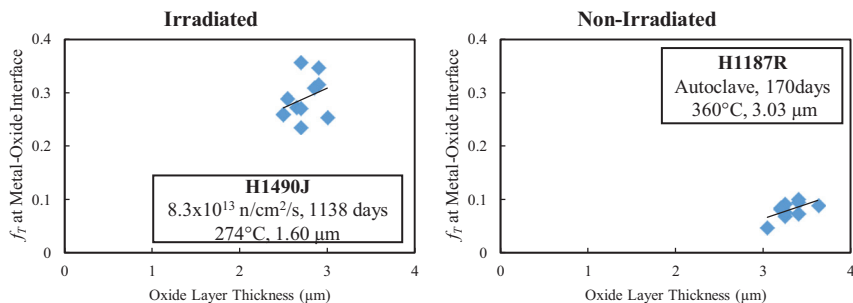
FIG. 17   Tetragonal fraction at the metal-oxide interface as a function of oxide thickness from XRD maps acquired on (left) H1490J (8.3 ×10^{13} n/cm^2/s, 1,138 days, 274°C, 1.60 μm) and (right) H1187R (autoclave, 170 days, 360°C, 3.03 μm).

distribution of f_T at the metal-oxide interface as a function of oxide thickness in that location (with a reproduced figure from Ensor et al.[9] alongside). Both sets of data show scatter with a slight increase of f_T with oxide thickness using best fits. The value of f_T from the irradiated Zircaloy-4 sample is higher (three to five times) than the nonirradiated sample, due to the neutron fluence. It is possible the proximity to transition could also be affecting the values here and causing some of the difference as the f_T values for the autoclave sample examined here were uncharacteristically small and are typically closer to ~ 0.15, as seen previously.[9] Differences in temperature have not been observed to impact the f_T observations for irradiated and nonirradiated testing (274°C versus 360°C in fig. 17), but it should be noted that metal texture (different for the two samples in fig. 17) was not included as a variable in this study; nevertheless, it was not observed to impact f_T in previous work using autoclave testing.[9]

The similarity in the oxide layers formed on samples corroded in an autoclave to samples formed on in-reactor corroded samples does provide some confidence that effects seen in autoclave corrosion correlate to in-reactor behavior. These similarities include diffraction peak χ location and intensity, the variation of the tetragonal fraction within the oxide layer, and the oxide grain size near the metal-oxide interface. Highlighted differences, such as the magnitude of the tetragonal fraction at the metal-oxide interface and the increase in monoclinic oxide grain size with exposure to neutron fluence, demonstrate in turn the importance of analyzing neutron-irradiated specimens to understand basic corrosion mechanisms and their role in phenomena such as the acceleration of oxide growth in reactor.

METALLOGRAPHIC EXAMINATION

Pretransition Oxide

The microstructure of the specimen examined using synchrotron XRD in figure 15 was also characterized by focused ion beam (FIB) serial sectioning. Optical imaging of the metallographic cross section showed the long-range variation in the oxide

film thickness (fig. 18). Some of the differences in film thickness likely result from the crystallographic orientations of different Zircaloy-4 grains.[25] A higher magnification, backscatter SEM image taken from the serial sectioning data set is also shown in figure 18. No cracks were observed in the oxide film, suggesting that transition did not occur at this location. Needle-like features were observed at the metal-oxide interface similar in appearance to those recently reported by others in Zircaloy-2 cladding obtained from a boiling water reactor.[26] A sister sample, H381J (fig. 1), that corroded for about twice the time and at a similar flux as the sample with the needles (H1490J), had 10 times the oxide layer thickness. The additional 10 times oxide thickness formed on H381J at exposure times beyond when H1490J was removed from testing (and at which point the needles were present). The high fluence of the sample, H1490J, on which the needles were observed (81.5×10^{20} n/cm^2) combined with the fact that this sample had not yet undergone the same rapid acceleration in corrosion at 274°C as its sister sample, H381J, could suggest that the needles are a precursor to unstable oxide growth. This morphology is similar to observations made on oxide layers of pure Zr prior to breakaway oxidation.[11,27]

Figure 19 is the three-dimensional rendering of a portion of the oxide film. The individual slices have a nominal resolution of 20 nm by 20 nm by 50 nm, and the dimensions of the reconstructed volume are 15.8 µm by 8.7 µm by 3.0 µm. Two distinct grooves (arrowed) were visible at the metal-oxide interface. Based on the BSE images, the grooves were found to follow the intersection of Zircaloy-4 grain boundaries with the metal-oxide interface and suggested that at least some of the needle-shaped protrusions resulted from enhanced oxidation along the grain boundaries.

FIG. 18   Top, optical image obtained from the metallographic cross section of H1490J (8.3×10^{13} n/cm^2/s, 1,138 days, 274°C, 1.60 µm). The oxide is visible as a thin, medium gray layer. Bottom, backscatter SEM image of the metal-oxide interface extracted from an FIB serial section.
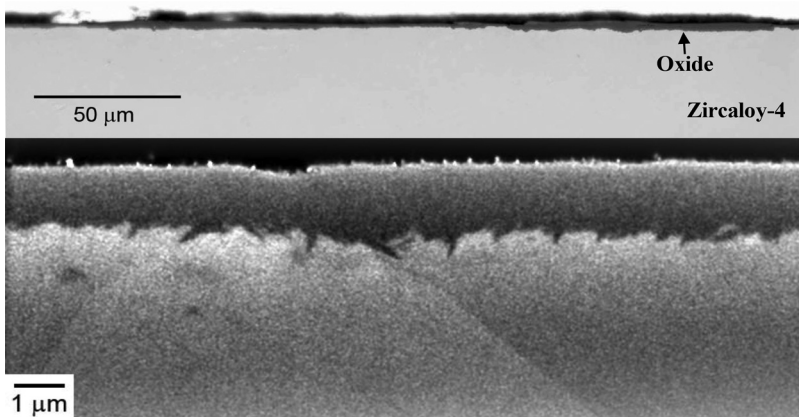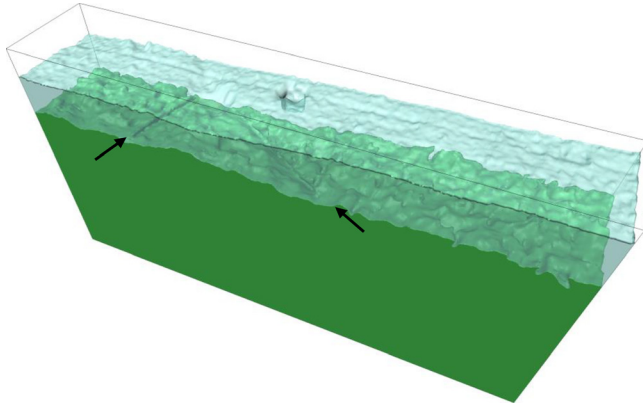

Oxide

Zircaloy-4

50 µm

1 µm

FIG. 19 FIB serial section reconstruction acquired on H1490J (8.3×10^{13} n/cm^2/s, 1,138 days, 274°C, 1.60 µm). Arrows mark the location of Zircaloy-4 grain boundaries intersecting the metal-oxide interface. The dimensions of the reconstructed volume are 15.8 µm by 8.7 µm by 3.0 µm. The oxide is rendered semitransparent to facilitate viewing of the metal-oxide interface, and the Zircaloy-4 is shown in green (and not transparent).

The traces of the grain boundary planes were also visible in the image shown in figure 19 (black arrows). The average thickness (h_{ave}) of the oxide was 1.50 µm, as measured from the reconstructed volume, and the range (h_{max} to h_{min}) was 1.6 µm. The root mean square (RMS) height of the metal-oxide interface was measured as 0.18 µm.

Post-Transition Oxides

Three post-transition oxide films were examined with the FIB-SEM serial-section technique. The dimensions of each serial section are listed in table 2. The nominal voxel dimensions were identical to those used for the pretransition specimen.

Optical images of two specimens corroded at 355°C to examine flux effects are shown in figure 20. The oxide films appear qualitatively similar at this magnification. Reconstructions of the oxide films from these two isothermal specimens are shown in figure 21.

TABLE 2 FIB serial-section parameters for the isothermal, post-transition specimens

Sample Designation	Avg. Flux (10^{13}n/cm^2/s) E > 1 MeV	x (µm)	y (µm)	z (µm)
H337J	0	12.5	34.3	10.8
H421J	1.4	17.1	33.1	6.1
H381J	10.5	10.6	23.7	5.7

FIG. 20   Optical images obtained from the metallographic cross sections of specimens H337J and H421J, showing the overall microstructure of the oxide film and metal-oxide interface.
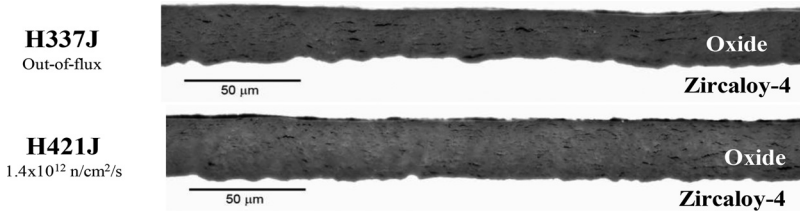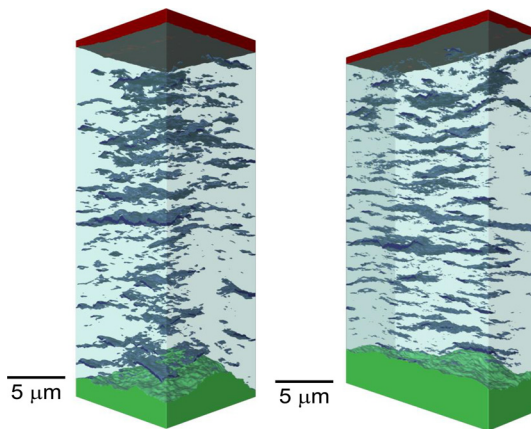

FIG. 21   Left, reconstructed FIB serial section acquired from H337J (zero flux, 1,139 days, 355°C, 25.6 μm), and right, H421J (1.4×10^{13} n/cm^2/s, 537 days, 355°C, 25.7 μm). The capping layer is red (top), the cracks are dark blue (in the middle), and the Zircaloy-4 is rendered in green (at the bottom). The oxide is semitransparent.

Qualitative observations of the two reconstructed volumes in figure 21 revealed a similar arrangement and size of cracks in the oxide films. Measurements of the volume fraction of cracks and RMS interface roughness are listed in table 3. The overall volume fraction of resolvable cracks in the oxides corroded at 355°C and shown in figure 21 were similar, approximately 0.024. However, the out-of-flux specimen showed a greater interface roughness over the area that was examined.

The similar average crack spacing in the oxide despite the higher corrosion rate of the in-flux sample suggests that the in-cycle corrosion kinetics, rather than the frequency of transition, was most influenced by the irradiation at this temperature. It is also notable that this sample had a low total neutron fluence (6.8×10^{20} n/cm^2). For a high neutron fluence sample (217.1×10^{20} n/cm^2) corroded at a lower

TABLE 3 Results from analysis of the reconstructed FIB serial-section data for the isothermal, post-transition specimens

Sample Designation	Avg. Flux (10^{13} n/cm^2/s) E > 1 MeV	Corrosion Temperature	Vol. Fraction Cracks	Metal-Oxide RMS Height (μm)
H337J	0	355°C	0.0237	0.69
H421J	1.4	355°C	0.0239	0.44
H381J	10.5	272°C	0.0510	0.38

temperature (272°C), significant differences in oxide microstructure were observed in the FIB-SEM data acquired. The oxide film on this specimen exhibited variation in both thickness and crack morphology (i.e., size and spatial distribution) as evidenced from the optical and SEM images shown in **figure 22**.

The cracking observed in **figure 22** does not show the heterogeneity that is characteristic of autoclave corroded specimens. While a layered crack structure still appears, it is more prevalent in locations of less oxide penetration, which is thought to be caused by uneven oxide growth stresses that result from a rapid irradiation induced breakaway oxidation. To better understand the crack spacing in the oxide,

**FIG. 22** Top, optical microscope image of metallographic cross section of specimen H381J (10.5 × 10^{13} n/cm^2/s, 2,395 days, 272°C, 15.8 μm). The oxide is the light gray layer. Bottom, backscatter SEM image of the metallographic cross section.
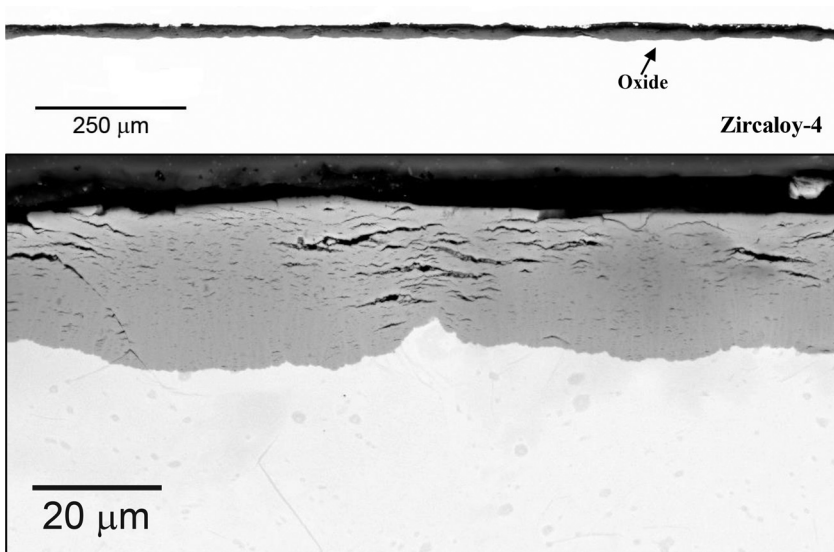
serial sectioning was performed. A representative image from the serial section and two views of the resulting reconstructed data are shown in **figure 23**. The average thickness of the oxide film in the area analyzed by serial sectioning was 21.9 μm, which was larger than the thickness of 15.8 μm based on weight gain; therefore, the region of this volume was likely acquired in a thicker portion of the oxide, which can vary as seen in **figure 22**.

Figure 23 shows that the cracks were inclined to the nominally flat starting surface of the specimen and suggest that the cracks formed along the contours defined by the metal-oxide interface as it evolved during corrosion. A coarse crack structure was found near the top of the oxide; this caused the volume fraction of resolved cracks to be 0.051, higher than the lower flux, higher-temperature specimens, as seen in **table 3**. The location of these cracks when compared to time (or dose) indicated that this portion of the film grew at the relatively low rate that accounted for most of the exposure. The rate acceleration that was observed at approximately 1,600 days ($\sim$ 26 dpa) corresponded with a change in this crack morphology. Specifically, the spacing between adjacent cracks decreased and the cracks generally became smaller in lateral size. The work on this high neutron fluence exposed

FIG. 23   Left, BSE SEM image extracted from the FIB serial section acquired from H381J (10.5×10^{13} n/cm^2/s, days, 271°C, 15.7 μm). Middle and right, images of the reconstructed serial section showing the capping layer (red, on top), cracks (blue, in the middle), and Zircaloy-4 (green, on the bottom). The oxide is rendered semitransparent.
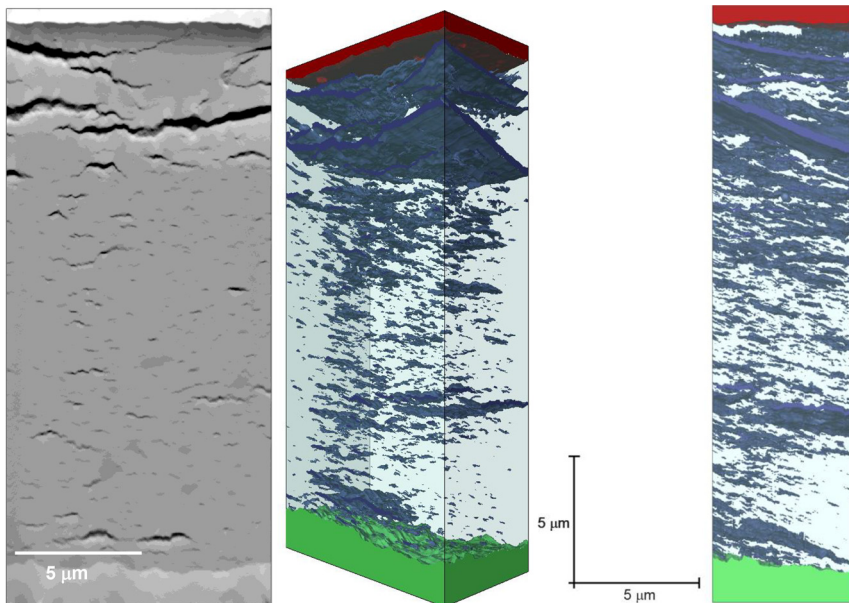
sample (and its corresponding high corrosion rate shown in fig. 1) compared to the samples exposed to less neutron fluence (but at higher temperatures) illustrates a different oxide morphology that may be a consequence of an irradiation-induced breakaway oxidation.

HYPOTHESIS ON THE IRRADIATION-INDUCED CORROSION TRANSITION OF ZIRCALOY-4 IN PILE

Kammenzind et al. provide details on corrosion experiments of Zircaloy-4 performed both under irradiation and in autoclave that suggest that the radiation environment acts synergistically with the corrosion film formed to cause the large enhancement of in-reactor corrosion rates, such as that observed in figure 1.[5] These findings are important to revisit in order to understand the results described in this paper. The synergism was hypothesized to occur due to irradiation effects on SPPs and the alloying element redistribution in the base metal structure combined with heterogeneous radiolysis effects within thick oxide films ($>$ 4 to 5 µm) and led to 30 to 40 times accelerated corrosion rates at temperatures between approximately 270°C and 310°C in samples similar to those examined in this paper. These large accelerations occur primarily in the post-transition regime. The radiation environment had little effect on the pretransition (protective barrier layer) corrosion kinetics; however, exposure to various levels of neutron fluence did shorten the time at which the material transitioned from pretransition to post-transition. Various models, such as the one put forth by Couet et al., can accurately describe the corrosion in the pretransition regime, and much work is ongoing in the further development of these models.[21] The two corrosion regimes (pretransition and post-transition) and the time at which the corrosion transitions from one to the other are the key descriptors of in-reactor Zircaloy-4 corrosion. It is noted here that there is a distinction between "transition to in-reactor post-transition corrosion kinetics" and the "transition" ascribed to cyclic behavior often observed out of reactor (which is responsible for the layered oxide structure that has been observed[11–13,15]). The former causes a much larger, persistent increase in corrosion rate than the latter (which leads to the formation of a new protective barrier layer) and is, therefore, the focus here, although it is possible the causes of both are related.

The work presented here provides the characteristics of the oxide formed on irradiated Zircaloy-4 that are needed for an investigation into the cause of its transition from pretransition to post-transition. The aforementioned thick film effects (e.g., heterogeneous radiolysis) could not cause a transition prior to the existence of the thick film and likely play a role in the magnitude of the acceleration once in the post-transition regime. The neutron fluence linked changes to the metal microstructure (SPPs and alloying element distribution) could not only accelerate corrosion in a post-transition regime (synergistically with other effects as described earlier) but may also contribute to the transition itself. This was demonstrated in an experiment by Kammenzind et al., which showed that Zircaloy-4 that had been previously exposed in reactor and then had the oxide film removed and the surface

reprepared would undergo transition sooner than material that had not been exposed.[5] The time at which the transition occurred was a function of the time and neutron fluence that the material had been exposed to throughout its life. Described in this paper, there was an observed relationship between the tetragonal-phase fraction at the metal-oxide interface and the neutron fluence, with a saturation effect taking place at approximately the same neutron fluence (~ 20 to 30×10^{20} n/cm^2) that the corrosion rate data in Kammenzind et al. showed a change in corrosion kinetics. As described here and in previous work,[9] the tetragonal phase presence could be an indicator of stress present at the metal-oxide interface. Thus, it is hypothesized that the ability of Zircaloy-4 metal to accommodate the oxide growth-induced stresses as it undergoes changes due to radiation could be the cause of the transition from the pretransition regime to the post-transition regime. Further testing is needed to understand and describe this mechanism in detail and how other alloy systems (such as zirconium-niobium) show resistance to this enhanced corrosion regime.

Conclusions

Eleven irradiated Zircaloy-4 specimens corrosion tested at different temperatures and fluence were studied using microbeam synchrotron radiation XRD and XRF (using a 0.2-µm microbeam permitting the examination of the oxide as a function of distance from the metal-oxide interface) and advanced characterization techniques (such as SEM, FIB serial sectioning, and XRD). The samples were corroded in reactor at a range of temperatures (272°C to 355°C) and neutron fluxes (0 to 11.5×10^{13} n/cm^2/s, E > 1 MeV) and to a variety of oxide thicknesses (1.6 µm to 29.3 µm). The conclusions of the experiments are as follows:

- The grain size calculated from peak broadening of the oxide peaks revealed that on oxide layers of irradiated Zircaloy-4 samples:
  - The monoclinic-phase grain size is higher for samples exposed to higher neutron fluxes and to higher neutron fluences. The monoclinic grain size grows continually away from the metal-oxide interface and has a dependence on corrosion temperature.
  - The average tetragonal grain size is constant as a function of temperature, neutron flux, and neutron fluence, suggesting that above ~ 15 nm, the tetragonal oxide phase is not stable and transforms to a monoclinic oxide phase in oxide layers formed on Zircaloy-4. This is supported by a decrease in f_T in the bulk oxide as a function of neutron fluence.
- The maximum f_T occurs near the metal-oxide interface and increases as a function of neutron fluence.
  - This increase saturates around ~ 30 to 50×10^{20} n/cm^2 and likely occurs because of irradiation hardening limiting the amount of stress the metal can accommodate, which leads to higher stress accumulation at the metal-oxide interface, which can lead to an increase in the tetragonal-phase fraction.

- The XRD examination revealed that the irradiated Zircaloy-4 samples had oxide peaks, intensities, and variations similar to the samples that were corroded in an autoclave, suggesting that the corrosion mechanisms in nonirradiated and irradiated Zircaloy-4 samples are similar.
- Two samples corroded at the same temperature (355°C) to the same final oxide thickness (~ 26 μm) but with different neutron exposures (zero flux for 1,139 days versus 1.4×10^{13} n/cm^2/s for 537 days) had similar oxide layer spacing and crack morphology despite the higher corrosion rate of the in-flux sample; this suggests that the in-cycle corrosion kinetics, rather than the transition oxide layer spacing, was most influenced by the irradiation at this temperature and low total neutron fluence (6.8×10^{20} n/cm^2).
- For one sample that was corroded at a low temperature (272°C) but experienced accelerated corrosion after ~ 26 dpa, the corrosion rate acceleration was correlated with a decrease in crack spacing and change in crack morphology that may be representative of an irradiated induced breakaway oxidation regime.

References

1. B. Cox, "Some Thoughts on the Mechanisms of In-Reactor Corrosion of Zirconium Alloys," *Journal of Nuclear Materials* 336 (2005): 331–368.
2. T. R. Allen, R. J. M. Konings, and A. T. Motta, "Corrosion of Zirconium Alloys," in *Comprehensive Nuclear Materials*, Vol. 5, ed. R. J. M. Konings (Oxford, UK: Elsevier, 2012), 49–68.
3. A. T. Motta, A. Couet, and R. J. Comstock, "Corrosion of Zirconium Alloys for Nuclear Fuel Cladding," *Annual Review of Materials Research* 45 (2015): 311–343.
4. P. Bossis, B. Verhaeghe, S. Doriot, D. Gilbon, V. Chabretou, A. Dalmais, J.-P. Mardon, M. Blat, and A. Miquet, "In PWR Comprehensive Study of High Burn-Up Corrosion and Growth Behavior of M5 and Recrystallized Low-Tin Zircaloy-4," *Journal of ASTM International* 6, no. 2 (2009): 1–27.

5.   B. F. Kammenzind, J. A. Gruber, R. Bajaj, and J. D. Smee, "Neutron Irradiation Effects on the Corrosion of Zircaloy-4 in a PWR Environment," in *Zirconium in the Nuclear Industry: 18th International Symposium*, ed. R. Comstock and A. Motta (West Conshohocken, PA: ASTM International, 2018), 448–490, https://doi.org/10.1520/STP159720160085

6.   C. Lemaignan and A. T. Motta, "Zirconium Alloys in Nuclear Applications," in *Materials Science and Technology: A Comprehensive Treatment*, Vol. 10B, ed. B. R. T. Frost (Weinheim, Germany: Wiley-VCH, 1994), 1–51.

7.   D. G. Franklin, "Performance of Zirconium Alloys in Light Water Reactors with a Review of Nodular Corrosion," *Journal of ASTM International* 7, no. 6 (2010): 1–15.

8.   R. Bajaj, B. F. Kammenzind, and D. M. Farkas, "Effects of Neutron Irradiation on the Microstructure of Alpha-Annealed Zircaloy-4," in *Zirconium in the Nuclear Industry: Thirteenth International Symposium*, ed. G. Moan and P. Rudling (West Conshohocken, PA: ASTM International, 2002), 400–426, 2001, https://doi.org/10.1520/STP11399S

9.   B. Ensor, D. J. Spengler, J. R. Seidensticker, R. Bajaj, Z. Cai, and A. T. Motta, "Microbeam Synchrotron Radiation Diffraction and Fluorescence of Oxide Layers Formed on Zirconium Alloys at Different Corrosion Temperatures," *Journal of Nuclear Materials* 526 (2019), https://doi.org/10.1016/j.jnucmat.2019.151779

10. H. Swan, M. S. Blackmur, J. M. Hyde, A. Laferrere, S. R. Ortner, P. D. Styman, C. Staines, M. Gass, H. Hulme, A. Cole-Baker, and P. Frankel, "The Measurement of Stress and Phase Fraction Distributions in Pre and Post-Transition Zircaloy Oxides Using Nano-Beam Synchrotron X-Ray Diffraction," *Journal of Nuclear Materials* 479 (2016): 559–575.

11. A. T. Motta, M. J. G. da Silva, A. Yilmazbayhan, R. J. Comstock, Z. Cai, and B. Lai, "Microstructural Characterization of Oxides Formed on Model Zr Alloys Using Synchrotron Radiation," *Journal of ASTM International* 5, no. 3 (2008): 1–20.

12. D. J. Spengler, A. T. Motta, R. Bajaj, J. R. Seidensticker, and Z. Cai, "Characterization of Zircaloy-4 Corrosion Films Using Microbeam Synchrotron Radiation," *Journal of Nuclear Materials* 464 (2015): 107–118.

13. A. Yilmazbayhan, A. T. Motta, R. J. Comstock, G. P. Sabol, B. Lai, and Z. Cai, "Structure of Zirconium Alloy Oxides Formed in Pure Water Studied with Synchrotron Radiation and Optical Microscopy: Relation to Corrosion Rate," *Journal of Nuclear Materials* 324 (2004): 6–22.

14. B. V. Cockeram, K. J. Leonard, T. S. Byun, L. L. Snead, and J. L. Hollenbeck, "Development of Microstructure and Irradiation Hardening of Zircaloy during Low Dose Neutron Irradiation at Nominally 377-440C," *Journal of Nuclear Materials* 449 (2014): 69–87.

15. E. Hillner, D. G. Franklin, and J. D. Smee, "Long-Term Corrosion of Zircaloy before and after Irradiation," *Journal of Nuclear Materials* 278 (2000): 334–345.

16. R. Adamson, F. Garzarolli, and C. Patterson, *In-Reactor Creep of Zr Alloys*, ZIRAT14/IZNA9 Special Topical Report (Mölnlycke, Sweden: ANT International, 2009).

17. A. T. Motta and C. Lemaignan, "A Ballistic Mixing Model for the Amorphization of Precipitates in Zircaloy under Neutron Irradiation," *Journal of Nuclear Materials* 195 (1992): 277–285.

18. F. Garzarolli, W. Goll, A. Seibold, and I. Ray, "Effect of In-PWR Irradiation on Size, Structure, and Composition of Intermetallic Precipitates of Zr Alloys," in *Zirconium in the Nuclear Industry: Eleventh International Symposium*, ed. E. Bradley and G. Sabol (West Conshohocken, PA: ASTM International, 1996), 541–556, https://doi.org/10.1520/STP16189S

19. M. Griffiths, J. F. Mecke, and J. E. Winegar, "Evolution of Microstructure in Zirconium Alloys during Irradiation," in *Zirconium in the Nuclear Industry: Eleventh International Symposium*, ed. E. Bradley and G. Sabol (West Conshohocken, PA: ASTM International, 1996), 580–602, https://doi.org/10.1520/STP16191S

20. F. Garzarolli, B. Cox, and P. Rudling, "Optimization of Zry-2 for High Burnups," in *Zirconium in the Nuclear Industry: 16th International Symposium*, ed. M. Limbäck and P. Barbéris (West Conshohocken, PA: ASTM International, 2011), 711–753, https://doi.org/10.1520/STP152920120028

21. A. Couet, A. Motta, and A. Ambard, "The Coupled Charge Compensation Model for Zirconium Alloy Fuel Cladding Oxidation, I. Parabolic Oxidation of Zirconium Alloys," *Corrosion Science* 100 (2015): 73–84.

22. B. Ensor, A. M. Lucente, M. J. Frederick, J. Sutliff, and A. T. Motta, "The Role of Hydrogen in Zirconium Alloy Corrosion," *Journal of Nuclear Materials* 496 (2017): 301–312.

23. R. Garvie and P. Nicholson, "Phase Analysis in Zirconia Systems," *Journal of the American Ceramic Society* 55 (1972): 303–305.

24. W. Qin, C. Nam, H. L. Li, and J. A. Szpunar, "Tetragonal Phase Stability in ZrO_2 Film Formed on Zirconium Alloys and Its Effects on Corrosion Resistance," *Acta Materialia* 55 (2007): 1695–1701.

25. G. Lucadamo and J. Gruber, "Investigating the Influence of Zircaloy-4 Grain Orientation on Oxide Corrosion Films Formed in an Autoclave Environment," *Microscopy and Microanalysis* 23, no. S1 (2017): 2200–2201.

26. A. Baris, R. Restani, R. Grabherr, Y.-L. Chiu, H. E. Evans, K. Ammon, M. Limback, and S. Abolhassani, "Chemical and Microstructural Characterization of a 9 Cycle Zircaloy-2 Cladding Using EPMA and FIB Tomography," *Journal of Nuclear Materials* 504 (2018): 144–160.

27. B. Ensor, "The Nature of Unstable Oxide Growth in Zirconium and Zirconium Alloys" (PhD thesis, The Pennsylvania State University, 2016).

Discussion

Question from Michael Preuss, University of Manchester:—I wonder if you can distinguish between the grain size of the metastable and stable tetragonal grain. As your tetragonal phase fraction does not drop to zero when these strain drop, you have size stabilized tetragonal grains and the second family is metastable tetragonal grains. If one assumes that the 2% stable tetragonal grains fraction is constant, one should be able to deconvolute the grain size analysis of the families in the stress stabilized region. It is a fairly simple mathematical exercise.

Authors' Response:—A deconvolution of the metastable grain size at the metal-oxide interface (for samples with ample bulk oxide to measure from) as suggested shows a range of tetragonal sizes from 17.5 to 25 µm (with an average of 21 µm), with higher values at higher neutron fluence.

Question from Johannes Bertsch, PSI:—Hydrides—especially at high burnup and at the metal-oxide interface—have an influence on the stresses; oxide cracks are close to those cracks. Is it considered in the model?

Authors' Response:—We agree this is a possibility at high burn-up. As described in Ensor et al.,[1] hydrogen can accelerate corrosion as more hydrides accumulate in the material. As shown in figure 1 here, the irradiation-induced transition occurred for the low-temperature specimen at a low weight gain ($\sim$ 50 mg/dm^2) and

correspondingly low hydrogen content that is not enough to substantially accelerate the oxide growth to the rates observed.

1.   B. Ensor, A. M. Lucente, M. J. Frederick, J. Sutliff, and A. T. Motta, "The Role of Hydrogen in Zirconium Alloy Corrosion," *Journal of Nuclear Materials* 496 (2017): 301–312.

Question from Philipp Frankel, UOM:—How can the observation/hypothesis that irradiation hardening plays a role in irradiation-enhanced corrosion compare to other previous observations that preirradiated samples do not show pretransition acceleration? Can oxide texture be inferred from the XRD data?

Authors' Response:—We do not hypothesize that irradiation affects pretransition kinetics but rather that it can accelerate the onset to irradiation-induced accelerated corrosion. In Kammenzind et al.,[2] the oxide layers were removed from samples irradiated to various levels and were subsequently reexposed in reactor, showing that the time to irradiation-induced transition is shortened, suggesting an impact of the irradiation on the metal.

The measurement of texture requires more analysis and tilting than was performed in this work. As far as we could tell, the oxide texture was similar to previous measurements.

2.   B. F. Kammenzind, J. A. Gruber, R. Bajaj, and J. D. Smee, "Neutron Irradiation Effects on the Corrosion of Zircaloy-4 in a PWR Environment," in *Zirconium in the Nuclear Industry: 18th International Symposium*, ed. R. Comstock and A. Motta (West Conshohocken, PA: ASTM International, 2018), 448–490, https://doi.org/10.1520/STP159720160085

Question from Philippe Bossis, CEA:—More than the total amount of tetragonal (phase), can the amount of destabilized tetragonal Zr be considered as a key parameter?

Authors' Response:—If the tetragonal phase can be used as a marker for stress at the metal-oxide interface, then yes.

Question from Hans-Olof Andren, Chalmers Univ. of Technology:—I'd like to emphasize the importance of lateral cracks of the oxide growth rate. These cracks are, of course, a consequence of a tensile stress perpendicular to the metal-oxide interface, caused by an undulating interface and the 55% oxide expansion, and they occur preferentially over metal hills in the interface as can be seen in your micrograph of 272°C irradiated Zy-4. We have reported[3] that each unoxidized SPP embedded in the oxide has a void adjacent to it that might act as a nucleation site for a lateral crack, and that a good distribution of small isolated cracks might make the stress lower in the oxide and thus delay crack joining and kinetic transition. There is also a lateral expansion of the oxide (some 0.5%) that generates tensile stress and plastic deformation in the underlying metal, and it may well be that

irradiation hardening of the metal increases the stress level in the oxide, leading to the earlier kinetic transition that you observe.

Authors' Response:—We agree that the lateral cracks are important in promoting percolation of porosity in the oxide. The prevalent stresses should cause lateral cracking as you observe.

3.   P. Tejland and H.-O. Andrén, "Origin and Effect of Lateral Cracks in Oxide Scales Formed on Zirconium Alloys," *Journal of Nuclear Material* 40 (2012): 64–71.